nature physics

SUPPLEMENTARY INFORMATION

DOI: 10.1038/NPHYS2848

Spin–layer locking effects in optical orientation of exciton spin in bilayer WSe_2

Aaron M. Jones, Hongyi Yu, Jason S. Ross, Philip Klement, Nirmal. J. Ghimire, Jiaqiang Yan, David G. Mandrus, Wang Yao, Xiaodong Xu

S1. Interlayer tunneling in the K valleys of AB stacked bilayers

We first analyze the band edge wavefunctions in the K valleys of two decoupled monolayers with AB stacking order. Here, the conduction band edges originate predominantly from the transition metal d_{z^2} orbital (with magnetic quantum number $m = 0$) [S1], and the Bloch function can be written as $\psi_{c\mathbf{K}}^{u,l} = \sum_n e^{i\mathbf{K}\cdot\mathbf{r}_n} d_{m=0}^{u,l}(\mathbf{r}_n)$. The vector $\mathbf{r}_n$ is the location of the n-th metal atom, and superscript u (l) denotes the upper (lower) layer. The valence band edges in the upper (lower) layer originate predominantly from the transition metal $d_{x^2-y^2} - id_{xy}$ ($d_{x^2-y^2} + id_{xy}$) orbital [S1] with magnetic quantum number $m = -2$ ($m = +2$). The corresponding Bloch function at **K** is then $\psi_{v\mathbf{K}}^{u} = \sum_n e^{i\mathbf{K}\cdot\mathbf{r}_n} d_{m=-2}^{u}(\mathbf{r}_n)$ ($\psi_{v\mathbf{K}}^{l} = \sum_n e^{i\mathbf{K}\cdot\mathbf{r}_n} d_{m=+2}^{l}(\mathbf{r}_n)$), and those at the –**K** point are just their time reversal.

Now we consider nearest neighbor interlayer hopping for the metal atoms, as shown in Fig. S1. The three pairs of interlayer hopping shown by the arrows in Fig. S1 are related by $2\pi/3$ rotations because of the crystal's three-fold rotational symmetry. The center upper layer atom has position **r**=0 while the positions of the three lower layer atoms are denoted as $\mathbf{r}_1$, $\mathbf{r}_2$ and $\mathbf{r}_3$. The hopping amplitude is proportional to the wave function overlap, given by $\sum_{n=1,2,3} e^{i\mathbf{K}\cdot\mathbf{r}_n} \langle d_{m=0}^{l}(\mathbf{r}_n) | d_{m=0}^{u}(0) \rangle$ for the conduction band, and $\sum_{n=1,2,3} e^{i\mathbf{K}\cdot\mathbf{r}_n} \langle d_{m=+2}^{l}(\mathbf{r}_n) | d_{m=-2}^{u}(0) \rangle$ for the valence band.

Writing $\mathbf{K} = \frac{4\pi}{3a}\hat{\mathbf{x}}$, then $e^{i\mathbf{K}\cdot\mathbf{r}_1} = 1$, $e^{i\mathbf{K}\cdot\mathbf{r}_2} = e^{-i2\pi/3}$ and $e^{i\mathbf{K}\cdot\mathbf{r}_3} = e^{i2\pi/3}$. $\langle d_{m'}^{l}(\mathbf{r}_2) | d_{m}^{u}(0) \rangle$ ($\langle d_{m'}^{l}(\mathbf{r}_3) | d_{m}^{u}(0) \rangle$) is then related to $\langle d_{m'}^{l}(\mathbf{r}_1) | d_{m}^{u}(0) \rangle$ through a $2\pi/3$ ($-2\pi/3$) rotation operation $\hat{\mathcal{R}}\left(\pm\frac{2\pi}{3}\right)$ on $d_m^u(0)$ and $d_{m'}^l(\mathbf{r}_1)$, where $\hat{\mathcal{R}}\left(\pm\frac{2\pi}{3}\right) d_m^{u,l} = e^{\mp i\frac{2\pi}{3}m} d_m^{u,l}$.

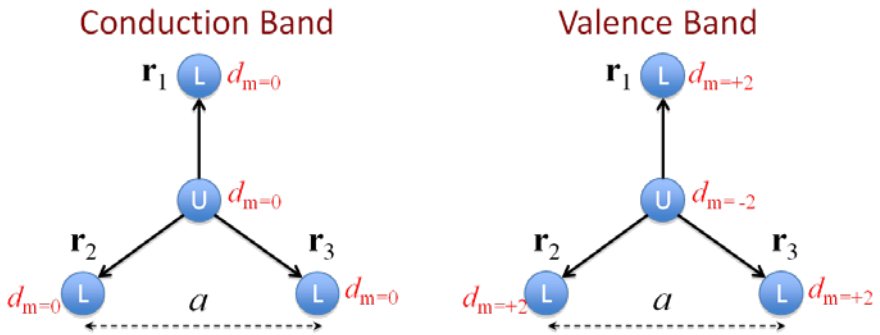

Figure S1| Nearest neighbor interlayer hopping of metal atoms at the K point in AB-stacked bilayers. Atoms located in the upper (lower) layer are indicated by U (L) while red labels indicate the corresponding orbitals of the K point band edge Bloch functions.

DOI: 10.1038/NPHYS2848

Since $m = 0$, $\langle d^l_{m=0}(\mathbf{r}_1)|d^u_{m=0}(0)\rangle = \langle d^l_{m=0}(\mathbf{r}_2)|d^u_{m=0}(0)\rangle = \langle d^l_{m=0}(\mathbf{r}_3)|d^u_{m=0}(0)\rangle$ and interlayer hopping for conduction electrons at the K point is:

$$\sum_{n=1,2,3} e^{i\mathbf{K}\cdot\mathbf{r}_n}\langle d^l_{m=0}(\mathbf{r}_n)|d^u_{m=0}(0)\rangle \propto \sum_{n=1,2,3} e^{i\mathbf{K}\cdot\mathbf{r}_n} = 0.$$

For the valence band $\langle d^l_{m=+2}(\mathbf{r}_2)|d^u_{m=-2}(0)\rangle = e^{i2\pi/3}\langle d^l_{m=+2}(\mathbf{r}_1)|d^u_{m=-2}(0)\rangle$ and $\langle d^l_{m=+2}(\mathbf{r}_3)|d^u_{m=-2}(0)\rangle = e^{-i2\pi/3}\langle d^l_{m=+2}(\mathbf{r}_1)|d^u_{m=-2}(0)\rangle$. Thus interlayer hopping for holes at the K point is finite:

$$\sum_{n=1,2,3} e^{i\mathbf{K}\cdot\mathbf{r}_n}\langle d^l_{m=+2}(\mathbf{r}_n)|d^u_{m=-2}(0)\rangle = 3\langle d^l_{m=+2}(\mathbf{r}_1)|d^u_{m=-2}(0)\rangle.$$

We note that the conduction band edge wavefunctions also have a small component of d_{xz} and d_{yz} orbitals [S1]. At the K points in WSe_2, they introduce an interlayer tunneling $t_\perp$~0.4 meV [S2]. However, the conduction band also has a spin splitting 2λ~40meV [S1]. In AB stacked bilayer, this splitting has a valley and layer dependent sign, and corresponds to the energy cost for the interlayer hopping (see Fig. 1 in main text). Such a large ratio of $2\lambda/t_\perp$ virtually suppresses interlayer hopping of conduction electrons near K points.

S2. Broadband monolayer and bilayer WSe_2 PL spectra

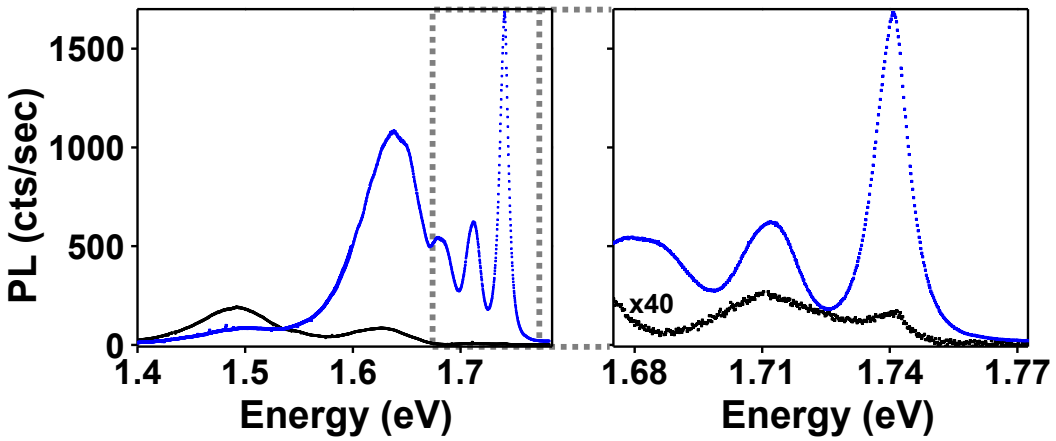

Figure S2| Comparison of monolayer and bilayer WSe_2 PL energies. Left panel: broadband PL spectrum of monolayer (blue) and bilayer (black) WSe_2. Right Panel: zoom-in of spectra within dashed boxed of left panel, showing bilayer WSe_2 data multiplied by a factor of 40. Emission at 1.74 eV for both monolayers and bilayers corresponds to X^o, while emission at 1.71 eV is from X^-.

S3. Broadband bi-WSe_2 differential reflectivity spectrum

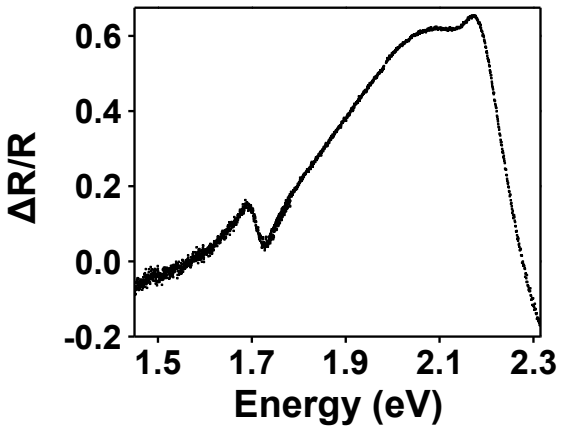

Figure S3| Broadband bi-WSe_2 ΔR/R spectrum. Broadband differential reflectivity spectrum for bi-WSe_2 at $V_g = 0$ showing the lowest energy absorption feature at ~1.7 eV.

S4. Gate dependence of bi-WSe_2 peak fitting parameters

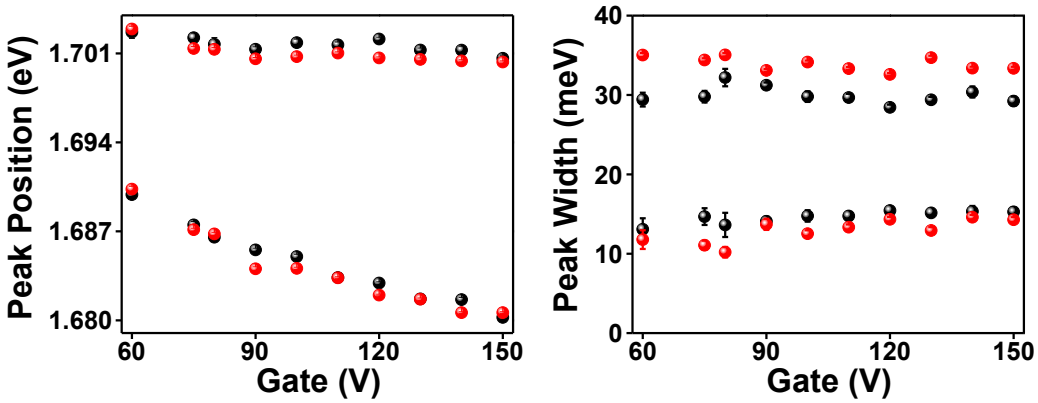

Figure S4| Gate dependence of doublet peak fitting parameters. Left panel: peak position as a function of gate voltage for split X^- peaks. Right panel: corresponding peak widths vs. gate voltage show little variation. Upper and lower data points correspond to peaks I and II, respectively (see main text), while black (red) points correspond to fits for circularly (linearly) polarized excitation.

DOI: 10.1038/NPHYS2848

S5. Second-harmonic generation in mono-, bi- and tri-layers of WSe_2

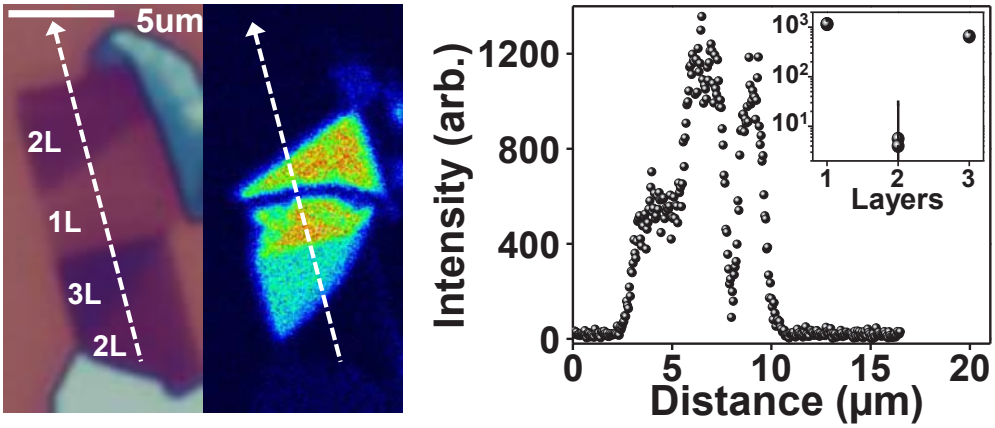

Figure S5| Layer-dependent second-harmonic generation. Left panel: optical microscope image of exfoliated WSe_2 with indicated layer number, alongside corresponding map of generated second harmonic intensity. Right panel: second harmonic intensity along line cut indicated by white dashed line in left panel. Inset: second harmonic intensity as a function of number of layers, showing contrast $>10^2$ between odd/even layers [S3-S5]. The line cut and inset plots show that the SHG signal from bilayers is within the noise of the background signal and can be ignored.

S6. Bilayer band structure in out-of-plane E-field

Following the discussions in section S1, at the $\pm\mathbf{K}$ points, the Hamiltonian of AB stacked bilayers in an out-of-plane electric field E can be written as [S6],

$$\begin{bmatrix} \Delta - \tau_z s_z \lambda_c + \frac{Ed}{2} & 0 & 0 & 0 \\ 0 & \Delta + \tau_z s_z \lambda_c - \frac{Ed}{2} & 0 & 0 \\ 0 & 0 & -\tau_z s_z \lambda_v + \frac{Ed}{2} & t_\perp \\ 0 & 0 & t_\perp & \tau_z s_z \lambda_v - \frac{Ed}{2} \end{bmatrix}.$$

The basis is $\left\{ \left|d^u_{z^2}\right\rangle, \left|d^l_{z^2}\right\rangle, \ 1/\sqrt{2}\left(\left|d^u_{x^2-y^2}\right\rangle - i\tau_z\left|d^u_{xy}\right\rangle\right), 1/\sqrt{2}\left(\left|d^l_{x^2-y^2}\right\rangle + i\tau_z\left|d^l_{xy}\right\rangle\right)\right\}$, where the superscripts "u" and "l" denote the "upper" and "lower" layer, respectively, with interlayer separation d. The monolayer band gap is denoted Δ, with λ_c (λ_v) the spin-valley coupling of electrons (holes) [S1]. Interlayer hopping for holes is $t_\perp$, whereas it vanishes for electrons. $\tau_z = \pm 1$ is the valley index of bilayer bands and s_z denotes the Pauli spin matrices. The out-of-plane electric field introduces an energy difference between the upper and lower layer, $\Delta_{Ec} = Ed$.

Holes at the K points then have eigenenergies $\pm\sqrt{(\tau_z s_z \lambda_v - Ed/2)^2 + |t_\perp|^2}$. Due to the large valence band spin splitting $2\lambda_v$, we focus only on the higher lying states at the band edge (the lower lying ones are hundreds of meV away). Hole states localized predominantly in the upper layer are:

$$|\downarrow\rangle'_{\mathbf{K}v} = \sqrt{1-|\alpha_1(E)|^2}|\downarrow\rangle_{u,\mathbf{K}v} + \alpha_1(E)|\downarrow\rangle_{l,\mathbf{K}v},$$
$$|\uparrow\rangle'_{-\mathbf{K}v} = \sqrt{1-|\alpha_1(E)|^2}|\uparrow\rangle_{u,-\mathbf{K}v} + \alpha_1(E)|\uparrow\rangle_{l,-\mathbf{K}v},$$

and have an eigenenergy $E_u = \sqrt{(\lambda_v + Ed/2)^2 + |t_\perp|^2}$; hole states largely localized in the lower layer are:

$$|\uparrow\rangle'_{\mathbf{K}v} = \sqrt{1-|\alpha_2(E)|^2}|\uparrow\rangle_{l,\mathbf{K}v} + \alpha_2(E)|\uparrow\rangle_{u,\mathbf{K}v},$$
$$|\downarrow\rangle'_{-\mathbf{K}v} = \sqrt{1-|\alpha_2(E)|^2}|\downarrow\rangle_{l,-\mathbf{K}v} + \alpha_2(E)|\downarrow\rangle_{u,-\mathbf{K}v},$$

and have an eigenenergy $E_l = \sqrt{(\lambda_v - Ed/2)^2 + |t_\perp|^2}$ (see Fig. S6). Here we use the shorthand notation $|\downarrow\rangle_{u,\mathbf{K}v} \equiv \frac{|d^u_{x^2-y^2}\rangle - i|d^u_{xy}\rangle}{\sqrt{2}} \otimes |\downarrow\rangle_{\mathbf{K}}$. The coefficients $\alpha_1(E) = t_\perp / \sqrt{\left(E_u + \lambda_v + \frac{Ed}{2}\right)^2 + |t_\perp|^2}$ and $\alpha_2(E) = t_\perp / \sqrt{\left(E_l + \lambda_v - \frac{Ed}{2}\right)^2 + |t_\perp|^2}$. The electric field thus induces a spin splitting at the valence band edge at the K points $\Delta_{Ev} = E_u - E_l$, which can be approximated as $\Delta_{Ev} \approx \frac{\lambda_v}{\sqrt{\lambda_v^2 + |t_\perp|^2}} Ed$ when $Ed \ll \lambda_v$, whereas for the conduction bands, we simply have the spin splitting $\Delta_{Ec} = Ed$. Our white light differential reflectivity measurements on monolayer WSe_2 show $2\lambda_v = 450$ meV, in good agreement with the first principle calculations in Ref. [S6] which give $2\lambda_v = 456$ meV. The same work extracts an interlayer hopping strength of $2t_\perp = 134$ meV for the valence band edges at the K points of bilayer WSe_2, from which we calculate $\Delta_{Ev} \approx 0.96\Delta_{Ec}$, and $\alpha_1(E) \approx \alpha_2(E) \approx 0.14$ for $Ed \ll \lambda_v$. The resulting difference between conduction and valence band shifts, $\Delta_{Ec} - \Delta_{Ev}$, contributes to the trion splitting observed at large gate voltages (see Fig. 3 and 4 in main text).

It should be noted that the interlayer hole hopping $t_\perp$ will induce a change in the direct band gap at the K points of bilayers from that of monolayers. At zero electric field, we have the band gap values $\Delta - \lambda_c - \lambda_v$ and $\Delta - \lambda_c - \sqrt{\lambda_v^2 + |t_\perp|^2}$ for monolayers and bilayers, respectively. In WSe_2, because of the large $\lambda_v/t_\perp$ ratio, we expect a small difference between the monolayer and bilayer direct band gap at K points: $\sqrt{\lambda_v^2 + |t_\perp|^2} - \lambda_v \sim 9$ meV, which is much smaller than the trion charging energy of ~30 meV. As a result, the resonances of excitons and trions formed at the K valleys of bilayers are nearly aligned with those of monolayers (Fig. S2). In contrast, in $MoSe_2$ the smaller value of $2\lambda_v = 182$ meV gives rise to a larger redshift of the exciton and trion lines in bilayers when compared to monolayers, as observed (see e.g. supplementary information of [S7]).

DOI: 10.1038/NPHYS2848

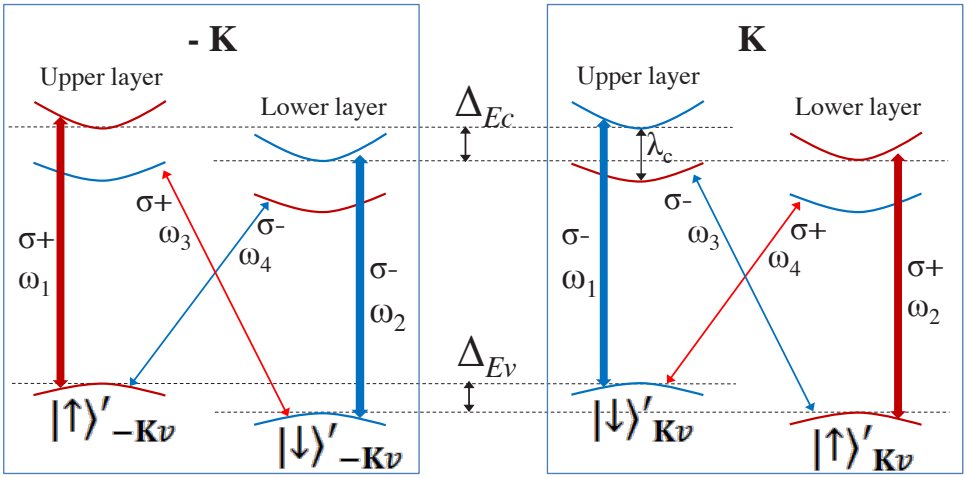

Figure S6| Band structure of bi-WSe_2 under applied electric field. The creation process of electron-hole pairs at resonances ω_1, ω_2, ω_3 and ω_4 via σ^+ (σ^-) polarized excitation is denoted by red (blue) double arrows. Arrow thickness denotes transition strength. Δ_{Ec} (Δ_{Ev}) is the interlayer conduction (valence) band splitting under the effect of an out-of-plane electric field.

S7. PL emission under circularly polarized excitation

An applied σ^+ (σ^-) polarized laser can excite electron-hole pairs through four transitions, as illustrated by red (blue) double arrows in Fig. S6. The arrow thickness denotes strength of the transition. The weak cross transitions denoted by thin arrows are due to the fact that the layer polarization of hole states near K points is ~96%, not fully polarized, a residual effect of the interlayer hopping.

Below we consider applying an incident laser with σ^+ polarization, which will excite electron-hole pairs through the four transitions denoted by the red arrows in Fig. S7. In emission, σ^+ PL will come predominantly from the two transitions marked by the thicker arrows with energies ω_1 and ω_2. Since the difference between Δ_{Ev} and Δ_{Ec} contributes to the difference between ω_1 and ω_2, in sufficiently large electric fields, this splitting may become resolvable.

The σ^- PL signal component is a consequence of electron spin relaxation (intra- and inter-valley). We expect that intra-valley spin relaxation is more efficient than inter-valley relaxation as the latter involves a simultaneous spin and valley flip. When Δ_{Ev} and Δ_{Ec} are much larger than the temperature, the spin relaxation channel from higher energy to lower energy states by phonon emission will also be much more efficient than the backward channel requiring phonon absorption. Thus the dominant spin relaxation channel is the one-way channel depicted by the green dotted arrow in Fig. S7. Therefore, we expect σ^- PL at resonance ω_2 to be much larger than at ω_1.

In summary, under σ^+ excitation we expect comparable σ^+ PL emission at both ω_1 and ω_2, while σ^- PL emission resulting from carrier spin relaxation is predominantly at

the lower resonance ω_2. When $\omega_1 - \omega_2$ is smaller than the peak linewidth, this manifests as a red shift of the σ^- PL.

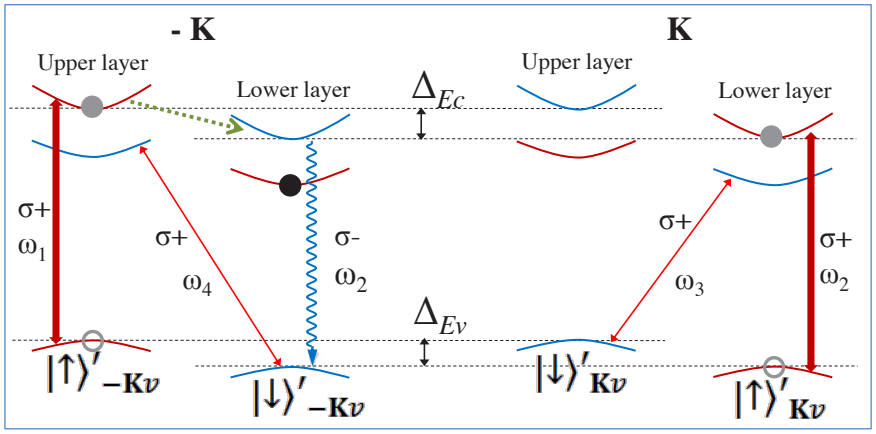

Figure S7| Allowed excitation and emission channels for σ^+ polarized excitation. Transitions driven by σ^+ polarized excitation are denoted by red arrows, with line thickness denoting transition strength. Gray circles denote photo-excited electron-hole pairs at either the K or -K valley. The black circle denotes the excess electron in X- trion configurations. The dominant emission channels are σ^+ polarized at frequencies ω_1 and ω_2. Emission of σ^- PL at ω_2 is indicated by the wavy blue arrow which becomes possible following the intra-valley spin flip of the photo-excited electron accompanied by emission of energy into the environment (green dashed arrow). The spin flipped electron can then recombine with holes photo-excited through the weak cross transition (ω_4) and emit a σ^- photon.

S8. X^- peak splitting

In the experiment a doublet peak feature is observed in the X^- spectrum for large gate voltages (main text Figs. 3a and 4a). We attribute this to the two different X^- configurations shown in Fig. S8a, where the X^- energy can be obtained from the X^o resonance by subtracting the trion charging energy. In the ω_1 configuration (top panel), the excess electron and the neutral exciton are in different layers (interlayer trion) and we write its charging energy as E_{c1}. In contrast, for the ω_2 configuration (bottom panel), the excess electron and neutral exciton are in the same layer (intralayer trion) and we write its charging energy as E_{c2}. Because of the layer separation, $E_{c1} < E_{c2}$ (see Fig. S8a). Thus, in the X^- spectrum the peak splitting is $\omega_1 - \omega_2 = (\Delta_{Ec} - \Delta_{Ev}) + (E_{c2} - E_{c1})$. Since the layer separation (7 Å) is comparable to the exciton Bohr radius (a_B~1 nm) [S8], and the monolayer trion charging energy is $E_{c2} \approx 30$ meV, we expect the charging energy difference $E_{c2} - E_{c1}$ can be as large as several meV.

In contrast, for the X^+ spectrum, the ω_1 configuration corresponds to *intralayer* trions with the excess hole and neutral exciton in the same layer (top panel Fig. S8b), and a charging energy E_{c1}. For the ω_2 configuration we have interlayer trions with the excess hole and neutral exciton in different layers (bottom panel Fig. S8b), and a charging energy E_{c2}. Now $E_{c1} > E_{c2}$, and the peak splitting is $\omega_1 - \omega_2 = (\Delta_{Ec} - \Delta_{Ev}) -$

DOI: 10.1038/NPHYS2848

$(E_{c1} - E_{c2})$, where the two contributions largely cancel. Consequently, the peak splitting $|\omega_1 - \omega_2|$ is larger for X^- than X^+ and thus more readily observed.

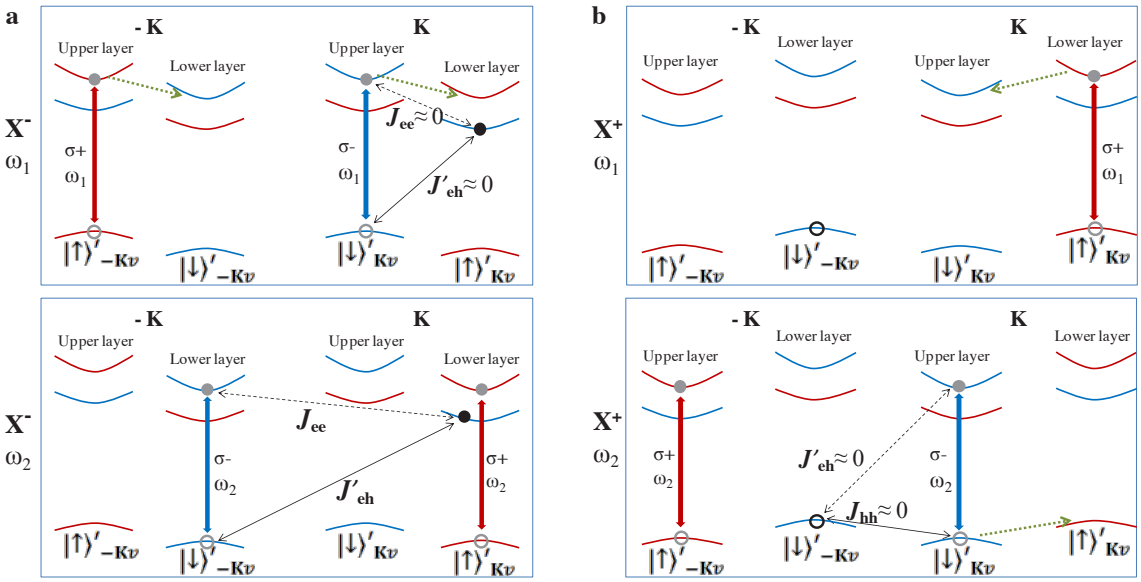

Figure S8| X^- and X^+ configurations under linearly polarized excitation. a, X^- configurations with emission energy ω_1 (upper panel) and ω_2 (lower panel), where an electron-hole pair (gray dot and circle) in a coherent superposition in the two valleys can lead to linearly polarized emission. Black dot denotes the excess electron in the lowest energy band (lower layer). Dashed green arrows represent spin relaxation processes and black double arrows indicate exchange interactions. Intervalley coherence at ω_1 (interlayer trions) is less affected by the excess electron than at ω_2 (intralayer trions) since the electron is on the layer opposite the recombining electron-hole pair. **b,** For X^+, the excess hole is in the lowest energy band (the lower layer). A coherent superposition in ±K valleys is not possible for intralayer positive trions at ω_1 (top panel) since the excess hole comprising the trion resides within the same layer, as in monolayers [S9]. For interlayer positive trions where the electron-hole pair is in the upper layer, opposite the excess hole (bottom panel), a valley superposition is allowed and experiences negligible exchange interactions.

S9. PL emission for linearly polarized excitation

A linearly polarized incident laser will create electron-hole pairs in a coherent superposition of states at K and –K. If the intervalley coherence can be preserved until electron-hole recombination, linearly polarized PL is emitted. Bilayers of transition metal dichalcogenides are qualitatively different from monolayers because of the additional layer degree of freedom. Below we analyze how valley coherence of a photo-excited electron-hole pair can be affected by the excess electron or hole in the X^- or X^+ configuration in bilayers. We consider the condition where the electric field induced Zeeman splitting between Δ_{Ev} and Δ_{Ec} is large, such that the excess electron (hole) is in the lower energy layer, as denoted by the black filled (open) circle in the lowest (highest) conduction (valence) band in Fig. S8a (Fig. S8b).

X^- emission occurs at either energy ω_1 or ω_2. We first look at the emission at ω_2 which comes from the intralayer trion configuration shown in lower panel of Fig. S8a, i.e. the photo-excited electron-hole pair (gray circles) is in same layer as the excess electron. Non-zero exchange interactions with the excess electron can destroy the intervalley coherence of the electron-hole pair, just as in the monolayer case [S9]. Hence, linear polarization is largely suppressed at this energy and one expects both co-polarized (i.e. identical to the excitation polarization) and cross-polarized (i.e. orthogonal to the excitation polarization) PL emission from intralayer trions. We now turn to X^- emission at ω_1, which comes from the interlayer trion configuration depicted in the upper panel of Fig. S8a. With the photo-excited electron-hole pair in the layer opposite the excess electron, the exchange interaction is substantially suppressed, such that intervalley coherence can be preserved and large linearly polarized PL can be observed at ω_1. This is in good agreement with the observed linear polarization behavior of the X^- doublet with applied gate.

In addition to the above exchange interactions which suppress linear polarization at ω_2, carrier spin relaxation as discussed in the previous section (green dotted arrows in Fig. S8a) will contribute unpolarized emission at ω_2 as well, further suppressing linearly polarized PL at this emission energy.

For the X^+ trion the situation is different. Emission at ω_1 is from the intralayer trion configuration shown in upper panel of Fig. S8b, where the photo-excited electron-hole pair is in the same layer as the excess hole. Similar to the monolayer case, because of the Pauli exclusion principle, X^+ PL cannot exhibit linear polarization at ω_1 [S9]. Emission at ω_2 is from the interlayer trion configuration shown in the lower panel of Fig. S8b, where the photo-excited electron-hole pair is in the layer opposite the excess hole. Linearly polarized emission is thus allowed at ω_2. As before, interlayer exchange interactions are strongly suppressed so that at this emission energy, the major depolarizing mechanism is the spin-relaxation of carriers denoted by the dotted green arrow.

S10. Supplementary References

S1 Liu, G.-B., Shan, W.-Y., Yao, Y., Yao, W. & Xiao, D. A three-band tight-binding model for monolayers of group-VIB transition metal dichalcogenides. *Physical Review B* **88**, 085433 (2013).

S2 Gui-Bin Liu, unpublished work.

S3 Kumar, N. *et al*. Second harmonic microscopy of monolayer MoS_{2}. *Physical Review B* **87**, 161403 (2013).

S4 Zeng, H. *et al*. Optical signature of symmetry variations and spin-valley coupling in atomically thin tungsten dichalcogenides. *Scientific reports* **3**, 1608 (2013).

S5 Malard, L. M., Alencar, T. V., Barboza, A. P. M., Mak, K. F. & De Paula, A. M. Observation of intense second harmonic generation from MoS_{2} atomic crystals. *Physical Review B* **87**, 201401 (2013).

S6 Gong, Z. *et al*. Magnetoelectric effects and valley-controlled spin quantum gates in transition metal dichalcogenide bilayers. *Nature Communications* **4**, 15 (2013).

S7 Ross, J. S. *et al*. Electrical control of neutral and charged excitons in a monolayer semiconductor. *Nature communications* **4**, 1474 (2013).

DOI: 10.1038/NPHYS2848

S8 Feng, J., Qian, X., Huang, C.-W. & Li, J. Strain-engineered artificial atom as a broad-spectrum solar energy funnel. *Nature Photonics* **6**, 866–872 (2012).

S9 Jones, A. M. *et al*. Optical generation of excitonic valley coherence in monolayer WSe2. *Nature Nanotechnology* 12 (2013).doi:10.1038/nnano.2013.151